The Pure Rotational Spectrum of Solvated HCl: Solute−Bath Interaction Strength and Dynamics

Bret N. Flanders, Xiaoming Shang, and Norbert F. Scherer*,†

Department of Chemistry, the James Franck Institute, and the Institute for Biophysical Dynamics, University of Chicago, 5735 S. Ellis Ave. Chicago, Illinois 60637

Daniel Grischkowsky

School of Electrical and Computer Engineering and Center for Laser and Photonics Research, Oklahoma State University, Stillwater, Oklahoma 74078

Received: June 18, 1999; In Final Form: August 5, 1999

A combination of pulsed THz transmission and FTIR spectroscopy was employed to measure the normalized frequency dependent absorption coefficient of HCl in spherical, dipolar, and linear solvents (CCl_4, $CHCl_3$, and alkanes, respectively) in the 0−350 cm^{-1} portion of the far-infrared spectral region. The analysis applied to the measured spectra describes the interaction between the quantum mechanical rigid rotator motion of HCl and the solvent through explicit consideration of the anisotropic potential between HCl and the bath. Nominally, the theory requires two adjustable parameters to fit the solvated HCl absorbance spectra. However, a compilation of experimental results for HCl dissolved in various solvents of high symmetry reveals a quadratic dependence of one parameter, the mean square field of the bath, on solvent polarizability. It is shown that dipole−induced dipole (DID) interactions account for the observed quadratic form. This observation introduces a constraint that reduces the number of adjustable parameters so that unique values for the second fitting parameter, the exponential decay rate of the anisotropic potential time correlation function, may be extracted from the measured absorbance curves. The analysis of HCl−alkane solution spectra reveals a more subtle aspect of this dependence. Only a very weak polarizability dependence was found for solvents of large aspect ratio such as the alkanes. This difference indicates that the *molecular polarizability density*, not simply the *molecular polarizability*, dictates the strength of the solvent mean square field. Last, a simple scheme for classifying nonpolar solvents based on DID interactions between the solute and the bath is established.

I. Introduction

Steady-state spectroscopic and structural investigations of liquids serve as an introduction to the difficult task of acquiring detailed knowledge of how solvents interact with reactants.[1,2] Such knowledge is important because during a chemical reaction the solvent strongly influences the possible reaction pathways.[3−7] Quantitative understanding of this influence would significantly impact our ability to predict chemical[8] and biological[9] reactivity in liquids. After a century of work to understand the details of condensed phase dynamics,[10−14] much more work is needed to connect the developing understanding of "homogeneous" condensed-phase environments to even more complex biological issues.

Steady-state[15−19] and time-resolved far-infrared (FIR) studies[20−22] of condensed phase dynamics are two general experimental approaches that are being developed to study chemical reactions in liquids. Both have significant merits. Time-resolved spectroscopy allows processes to be studied in "real time" and, thereby, helps to discriminate between the many different dynamical contributions to a time-averaged spectrum. Optical pump-far-infrared−probe spectroscopy methods are, in principle, sensitive to reaction-induced solvent motion (e.g., rotational and translational) in the vicinity of the chromophore. The time-resolved monitoring of this solvent reorganization is essentially a study of linear response theory.[23] However, measuring time-resolved far-infrared spectra of reactive solutions is technically quite demanding. Furthermore, few analytical methods for reliable interpretation of the time-resolved data have been developed.[24] Both of these challenges currently impede the progress of such studies of condensed phase reaction dynamics. However, the identification of reliable analysis methods for studies of transient spectra is logically developed through analysis of steady-state spectra. That is, for cases in which linear response theory and the fluctuation−dissipation theorem are valid, the equilibrium time-correlation function (or spectral density) corresponding to an experimental observable is connected to the nonequilibrium time-correlation function.[25,26] In such cases, knowledge of the equilibrated solute−solvent system can be directly related to understanding nonequilibrium spectra.

Investigations of gaseous systems often yield extremely detailed descriptions of the processes that occur in the molecular samples. A recent pulsed terahertz study of gaseous methyl chloride presents data so rich in spectral structure that an anomalous absorption around 1THz can be conclusively assigned to tunneling of the halide atom through the molecule.[27,28] The detailed analysis of condensed phase systems is more problematic because the magnitude and frequency of fluctuating intermolecular interactions characteristic of the liquid state "wash out" most spectroscopic information; rotational fine

* Corresponding author, E-mail: nscherer@rainbow.uchicago.edu.
† National Science Foundation National Young Investigator.

10.1021/jp992036n CCC: $18.00
Published on Web 11/20/1999

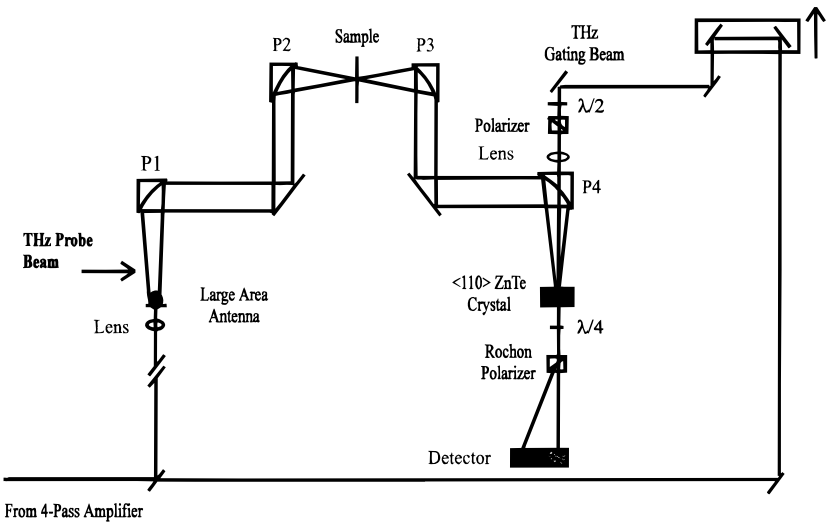

Figure 1. A schematic of the THz probe spectrometer. The single black line indicates the path taken by optical beams and the double black lines mark the path followed by the THz beam. P1−P4 refer to paraboloidal reflectors. $\lambda/2$ and $\lambda/4$ denote half and quarter wave plates for 800 nm radiation.

structure is absent. Still, rotational band contour analysis can yield useful information.

In a recent study,[16] Mori line shape functions[14] were used to analyze the structureless far-infrared absorption coefficient spectra of neat $CHCl_3$ and CCl_4. The spectra could only be successfully fit by using two Mori line shapes.[14,29] As a result, only two independently adjustable parameters were required to characterize the Bi−Mori line shape: a weight for each Mori line shape (A and 1-A) and the decay rate of the intermolecular torque auto-correlation function. The parameters for the two-lineshape fit indicate that (at least) two classes of molecular motion, diffusive (slow) and inertial (fast), give rise to the spectra. However, the formalism lacks detail about the quantum mechanical nature of the observed spectrum; this approach is limited to information about the time-scales for different types of molecular motion. Still, the torque correlation decay rate is of fundamental interest.[30]

A quantal theory for the analysis of rotational spectra in dense media has been developed and applied to the analysis of HCl solvated in a variety of simple solvents.[31,32] This formalism employs a quantum mechanical rigid-rotator line shape broadening model that allows simulating the solvated HCl spectra. Condensed phase environmental effects on the dynamics of HCl, manifested as strong line broadening and peak shifting of spectral features, are addressed through consideration of the anisotropic potential between an HCl molecule and the surrounding solvent molecules.[33] Generally, the anisotropic potential between the solute and the bath is characterized phenomenologically since the potential function of the analogous van der Waals molecule has not been measured or fully characterized. Hence, the solvated HCl absorbance spectra are fit using two adjustable parameters: τ_C, the exponential time constant characterizing the anisotropic potential time correlation (APTCF) function and λ^2, essentially the mean-square electric field exerted by the bath on HCl.

A provocative issue in the present study of solvated HCl, and in condensed phase studies in general, is to use gas phase spectral information to quantitatively understand condensed phase systems.[34,35] Being a diatomic molecule with a large rotational constant, HCl has a relatively sparse far-infrared spectrum. Therefore, the spacings between individual rotational transitions are comparable with line broadening due to interactions with the bath. Solvent dependent studies of λ^2 are presented for two classes of solvents: "spherical" and alkanes. Evidence for the importance of dipole−induced dipole (DID) interactions in both classes of solvents is presented. A quadratic solvent polarizability dependence of the mean square field parameter that is predicted by electrostatic theory is found for the spherical solvents. Thus, a physically meaningful constraint is established for λ^2 that reduces the arbitrariness associated with the multi-parameter model. As a result, unique values for τ_C may be extracted from the fitted solvated HCl absorbance curves.

This paper is organized as follows. A description of the experimental apparatus, including the home-built pulsed THz spectrometer, is presented in section II. Section III summarizes the theory used to model the measured spectra. The fitted curves for solvated HCl are presented in section IV, and the physical details of solvation evident in these data are discussed in section V. Conclusions are made in section VI.

II. Experimental Section

A. Pulsed Terahertz Apparatus and Measurement. The measurements of the liquid samples were performed with a home-built terahertz spectrometer driven by the amplified output of a cavity-dumped Ti:Sapphire oscillator.[36,38,39] The home-built, cavity-dumped oscillator is based on the standard four-mirror Kerr-lens mode-locked Ti:Sapphire oscillator[40,41] and is capable of generating sub-20 fs pulses.[36−38] The 0.2 mW 4 kHz cavity-dumped pulse train was directed to a grating/parabolic mirror pulse stretcher, where the temporal width of the pulses was stretched to roughly 9 ps. These low-peak energy pulses were then sent into a four-pass amplifier and subsequently compressed to pulses less than 200 fs in duration. The average power of the 4 kHz compressed pulse train was 20 mW, yielding 5 μJ pulses.

These pulses were directed into the THz time domain spectrometer shown in Figure 1; the optical beam was split into THz source and detection beams, each with average power of 1.0mW (250nJ/pulse) and were directed into the THz spectrometer. Because this spectrometer is powered by a low repetition rate train of moderately high energy pulses, modifications in the design of more conventional pulsed terahertz spectrometers have been made.[42,43] The high performance "F-chip" GaAs antenna sources[42,43] used in our previous studies[16,39] could not be used with amplified optical pulses; focusing even

a fraction of the available pulse energy onto the narrow 80 μm gap between transmission lines resulted in circuit burnout when a dC bias was applied. Therefore, GaAs antenna structures with an Ag transmission line separation of 5 mm that allowed illumination by the unfocused 3 mm diameter beam were employed.[44] A bias of up to +4.5 kV could be applied before circuit burnout occurred. The 780 nm above band gap pulse produced a sudden population of carriers in the 5 mm gap. Acceleration of photogenerated carriers under the applied bias gave rise to emission of THz radiation in an approximately toroidal volume about the axis of the carrier current acceleration. A detailed characterization of these large area antenna structures may be found elsewhere.[45]

A paraboloidal−flat−paraboloidal combination of Au-coated mirrors is used to collimate and focus the beam of THz pulses into the sample. A similar combination of optics is used to collect, direct and focus the THz beam into a 1.5 mm thick ⟨111⟩ ZnTe electrooptic sensor, where the THz signal is detected via the Pockel's effect.[46,47] Figure 2a shows the time-domain electric field profile of the THz pulse generated and detected in this spectrometer and Figure 2b illustrates the magnitude spectrum of the THz pulse. Usable intensity is available in the 3−90 cm^{-1} spectral region.

B. FTIR Apparatus. An FTIR spectrometer (BioRad FTS 6000) was used to measure the absorbance spectra of the HCl solutions in the 100−600 cm^{-1} region. A mercury arc lamp functioned as the source for far-infrared radiation and a 6.25 μm Mylar beam splitter was employed. The transmitted far-IR radiation was detected in a DTGS (deuterated triglycine sulfate) detector that was fitted with polyethylene windows for optimal transmission of the far-IR radiation. All compartments in the FTIR spectrometer were purged with dry nitrogen. The spectral response of the FTIR spectrometer is shown in Figure 2c.

C. Sample. The sample cell, composed of a machined stainless steel ring (10.0 mm thick, 6.0 cm inner diameter) sandwiched between two 1 mm thick zone refined Si windows, was inserted between the two focusing paraboloids, thereby allowing transmission measurements with the beam of terahertz radiation (0.1−3.0 THz, 3−100 cm^{-1}). Each spectrum is the result of twelve 256 data point scans over an 8 ps temporal window—each scan requiring 6 min for acquisition. The gaseous HCl sample was prepared by flowing a gentle stream of HCl gas into the cell for three minutes. The partial pressure of the gas in the cell approached 1 atm, but this number was not quantitatively determined. The solution of HCl in CCl_4 was prepared by bubbling HCl into roughly 150 mL of CCl_4 in an Erlenmeyer flask for 2 min. The concentration of the HCl/CCl_4 solution was then determined by measuring the vibrational absorbance spectrum of solvated HCl in the 2600−3100cm^{-1} spectral region where the absorption coefficients are known.[48] Hence, from Beer's law the HCl concentration was determined to be 0.08 M. It should be noted that spectral features around 2914 cm^{-1} resulting from the dimerization of HCl molecules were not observed.[49] The alkane solvated HCl systems were prepared analogously to HCl, but strong C−H bond absorption in the 2850−2960 cm^{-1} spectral region prevented quantitative spectroscopic determination of the HCl concentration. All measurements were performed at 296 K.

D. Solvated HCl Spectra. The low-frequency region (10−80 cm^{-1}) of the absorption coefficient and absorbance spectra are obtained by pulsed THz spectroscopy. Three separate pulsed THz measurements are required to obtain the spectrum of solvated HCl: the THz pulse transmitted through the empty sample cell, $E_{ref}(t)$; through the cell filled with the neat solvent, $E_{neat}(t)$; and through the cell filled with the HCl/solvent solution, $E_{soln}(t)$. Each of these time domain measurements is obtained by averaging eight individual 128 point scans of 8 ps in length. These signals are processed by a lock-in amplifier (Stanford Research Systems SR830) using a 300 ms time constant. Optical stability of the pulsed THz spectrometer must be maintained during these three measurements in order to achieve reliable results. The absorbance spectrum is calculated from the transmission ratio of the sample and the reference signals:[42] $\mathrm{Abs}(\omega) = -(2/l)\ln|[E_{samp}(\omega)/E_{ref}(\omega)]$ where l denotes the path length of the sample cell and $E(\omega)$ denotes the Fourier transform of the time domain electric field profile of the transmitted THz pulse $E(t)$. This time domain transmission profile is the actual quantity measured in pulsed THz spectroscopy. For the neat liquid, the expression for the absorbance spectrum is equivalent to that for the absorption coefficient spectrum. The absorbance spectrum for the HCl/solvent solution is determined as

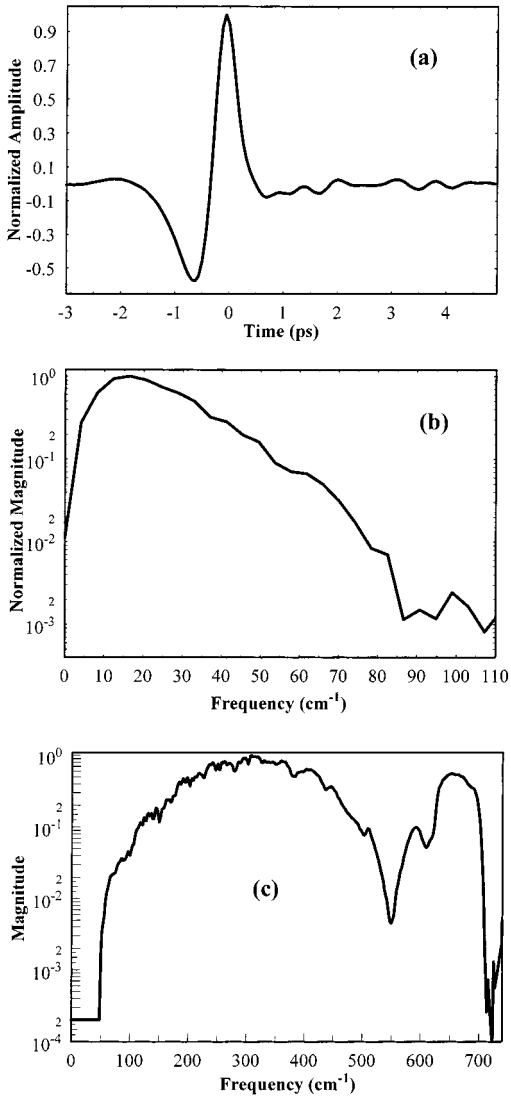

Figure 2. (a) The temporal profile of the amplifier-powered THz pulse after passage through an empty sample cell with Si windows. Reflective losses due to the high refractive index Si account for a roughly 50% reduction in the strength of the THz pulse upon transmission through the empty cell. The signal-to-noise ratio of the transmitted pulse is >500:1. (b) The normalized magnitude spectrum of the amplifier powered THz pulse detected by a ZnTe electro-optic sensor is denoted by a heavy line. The noise floor of the THz spectrometer is indicated by the plateau beginning at frequencies above 100 cm^{-1} and has a value of 1×10^{-3}. (c) The normalized magnitude spectrum of the FTIR spectrometer characterized by a mercury source and a DTGS detector.

$Abs_{HCl}(\omega) = -(2/l)\ln[E_{soln}(\omega)/E_{neat}(\omega)]$ where $E_{neat}(\omega)$ is the amplitude spectrum of the neat solvent and $E_{soln}(\omega)$ is the amplitude spectrum of the HCl/solvent solution. The absorption coefficient can be extracted from the measured data with knowledge of the concentration of HCl in the solution.

Three measurements are also required for the high-frequency regions (above 100 cm^{-1}): measurement of a reference spectrum (i.e., of the empty cell), measurement of the absorbance spectrum of the neat solvent, and measurement of the absorbance spectrum of the HCl solution. The FTIR-measured absorbance spectra are obtained analogously to the pulsed THz-measured spectra except that the data manipulation is performed by a commercial software program (Bio-Rad Win-IR Pro, Version 2.5).

III. Summary of Anisotropic Potential Spectral Theory

A. Quantum Mechanical Description of Solute Absorbance Spectra. The linear power absorption coefficient is proportional to the Fourier transformation of the HCl dipole moment time correlation function.[50] This frequency dependent quantity for a dilute solution of polar HCl molecules solvated by a nonpolar solvent is[50]

$$\alpha(\omega) = \frac{4\pi n\omega}{3\hbar c}(1 - e^{-\beta\hbar\omega})\mathrm{Re}[\int_0^\infty e^{i\omega t}\langle\mu(t)\mu(0)\rangle \mathrm{d}t] \quad (1)$$

where β is $1/k_B T$, n denotes the refractive index at frequency ω in the solution, and c is the speed of light in a vacuum. The angled brackets denote an ensemble average over the time-dependent product of $\mu(0)$ and $\mu(t)$ where μ is the vector dipole moment of HCl. The dipole moment TCF shown in eq 1 may be expressed in terms of the density matrix for the HCl−bath system,[51,52] yielding

$$\alpha(\omega) = \frac{4\pi n\omega}{3\hbar c}(1 - e^{-\beta\hbar\omega})\mu^2 \sum_{\chi}\sum_{\substack{i,f \\ f>i}} \sigma_i^0 \mathbf{u}_{\chi,f,i} \sum_{\substack{i',f' \\ f'\neq i'}} \mathbf{u}_{\chi,f',i'} Re[\sigma_{f,i}^{(f',i')}(\omega)] \quad (2)$$

for the frequency dependent absorption coefficient in terms of the reduced density matrix $\boldsymbol{\sigma}_{f,i}^{(f',i')}$. In eq 2, $\mathbf{u}_\chi$ is the unit vector associated with μ oriented with respect to a vector connecting the HCl center-of-mass to the bath molecule χ. The notation $\mathbf{u}_{\chi,f,i}$ denotes $\langle f|\mathbf{u}_\chi|i\rangle$ where $\langle f|$ and $|i\rangle$ are the rigid rotator eigenfunctions of HCl in states f and i, respectively. The second set of HCl rotational state indices f' and i' allow for summation over the frequency dependent density matrix $\sigma_{f,i}^{(f',i')}(\omega)$, independent of the summation over the steady-state density matrix σ_i^0, the population of the ith rotational level.

The effect of the bath molecules on the dynamics of the HCl dipole moment has been absorbed into the reduced density matrix operator $\sigma_{f'i'}^{(f,i)}(t)$, the fundamental dynamical quantity in this formalism as shown in eq 3. The equation of motion for the time dependent reduced density matrix operator, the non-Markovian master equation, can be expressed in a basis composed of system (HCl) eigenstates in the system−bath description as[31]

$$\dot{\sigma}_{f,i}(t) = -i\omega_{f,i}\sigma_{f,i}(t) - \sum_{f',i'}\int_0^t \hat{W}_{f,i;f',i'}(t-\tau)\sigma_{f',i'}(\tau)\mathrm{d}\tau \quad (3)$$

where the dot over $\sigma_{f,i}(t)$ represents the first time derivative, and the frequency factor ω_{fi} denotes the difference $(\omega_f - \omega_i)$. The convolution integral relates the current value for the rate of change of $\sigma_{f',i'}^{(f,i)}(t)$ to previous values of $\sigma_{f',i'}^{(f,i)}(\tau)$, i.e., acts as a memory term. The bath-induced dynamics of $\sigma_{f',i'}^{(f,i)}(t)$ are described solely by this memory term containing $W_{f,i;f',i'}(t)$, a fourth rank tensor. The elements of $W_{f,i;\,f',i'}(t)$ are the rates of bath-induced processes undergone by the ensemble of solvated HCl molecules. These processes are summarized as follows: $W_{i,i;f,f}(t)$ denote the rates for transition of population from level f to level i, $W_{f,i;f,i}(t)$ denote the rates for coherence dephasing between two levels f and i, $W_{f,i;f',i'}(t)$ denote the rates of coherence transfer from states f' and i' to states f and i.[52,53] Solute−bath interactions perturb the HCl wave functions and, thereby, couple HCl rotational states that would not be coupled in the absence of the perturbation.

Explicit characterization of the interaction between the solute and the bath molecules is made through calculation of the anisotropic potential time correlation function (APTCF) for the bath. $W_{f,i;f',i'}(t)$ is a sum of terms composed of these bath TCFs[54]

$$\hat{W}_{f,i;f',i'}(t) = \hbar^2(\delta_{i',i}\sum_{f''} e^{-i\omega_{f''}t}\langle H'_{f,f''}H'_{f'',f'}(t)\rangle + \delta_{f,f'}\sum_{i''} e^{-i\omega_{f,i''}t}\langle H'_{i',i''}H'_{i'',i}(t)\rangle) - e^{-i\omega_{f,i'}t}\langle H'_{i',i}H'_{f,f'}(t)\rangle - e^{-i\omega_{f',i}t}\langle H'_{i',i}H'_{f,f'}(t)\rangle \quad (4)$$

where i'' and f'' are additional indices for the rotational states of HCl. The probability amplitude for bath-(anisotropic potential) induced transitions between states i and f is[33]

$$H'_{fi} = \langle f|H'|i\rangle \quad (5)$$

and the anisotropic potential H' is[33,23]

$$H' = -\mu\cdot\vec{E} \quad (6)$$

where μ, the permanent dipole moment on HCl, is dotted into E, the electric field at the position of the HCl molecule due to the surrounding bath molecules.

Although molecular dynamics simulation of the HCl solution in principle allows explicit calculation of the APTCF, details regarding the interaction potential between HCl and individual solvent molecules are required. While this information may be experimentally determined for simpler systems such as HCl−Ar, the analogous information is not yet available for polyatomic solvents such as CCl_4 and alkanes. Therefore, a single-exponential function is used to describe the decay of the APTCF,[33] and use of eqs 5 and 6 allows expansion of the APTCF terms appearing in eq 4 to give the form:

$$\langle H'_{f,i}H'_{f',i'}(t)\rangle = \lambda_n^2\sum_{\chi}\mathbf{u}_{\chi,f,i}\mathbf{u}_{\chi,f',i'}e^{t/\tau_{C,n}} \quad (7)$$

In fitting the theoretical line shape to the measured data, λ_n^2 and $\tau_{C,n}$ are the nonreduced adjustable parameters (discussed further below) such that $\lambda_n^2 = {}^1/_3\mu^2\langle E^2\rangle$ and $\langle E^2\rangle$ is the mean-square field exerted by the bath on HCl. The sum runs over the configuration of solvent molecules surrounding HCl that induce the coupling between rotational states i and f (and i' and f'). The factor of ${}^1/_3$ arises because of the orientational averaging over the individual intermolecular interactions between the solute and the bath at thermal equilibrium. The probabilities associated with these bath-induced couplings are calculated by converting the sum into the appropriate 3-j coefficient.[33,55]

B. Secular and Nonsecular Components of the Absorbance Spectrum. Solving the first-order inhomogeneous differential equation appearing in eq 3 by Laplace−Fourier transformation techniques[56] yields[31]

$$\bar{\sigma}_{f,i}(\omega) = \frac{i\sigma_{f,i}(0)}{\omega - \omega_{f,i} + i\hat{\bar{W}}_{f,i;f,i}(\omega)}[1 - i\sum_{f',i'\neq f,i}\hat{\bar{W}}_{f,i;f',i'}(\omega)\bar{\sigma}_{f',i'}(\omega)] \quad (8)$$

for the frequency-dependent reduced density matrix where the overbar denotes the Laplace−Fourier transformed quantity. The terms due to the sum over f', i' differ widely in strength. The largest correspond to the case where $f, i = f', i'$ and are called *secular* terms. The remaining terms where $f, i \neq f', i'$ are called *nonsecular* and are strongest in the wings of an individual line where the overlap with neighboring spectral lines is strongest. Physically, these terms describe absorption effects resulting from the bath-induced transfer of population or coherence between the two neighboring sets of states f, i and f', i'.

Substitution of eq 8 into eq 3 yields a two component expression for the frequency dependent absorption coefficient.[31] The secular contribution is

$$\alpha_0(\omega) = \frac{4\pi n\omega}{3\hbar c}(1 - e^{-\beta\hbar\omega})\mu^2 Z_0^{-1}\sum_{i=0}(i+1)e^{-\beta\hbar cBi(i+1)}Re[\Lambda_{i+1,i}(\omega)] \quad (9)$$

where Z_0 is the rotational partition function.[69] The nonsecular contribution is

$$\alpha_1(\omega) = \frac{4\pi n\omega}{3\hbar c}(1 - e^{-\beta\hbar\omega})\mu^2\sum_{f,i}\sum_{\chi}\sigma_i^0\mathbf{u}_{\chi,i,f}\sum_{f',i'}\mathbf{u}_{\chi,i',f'}\cdot Re[\hat{\bar{W}}_{f',i';f,i}(\omega)\Lambda_{f',i'}(\omega)\Lambda_{f,i}(\omega)] \quad (10)$$

where the function $\Lambda_{f,i}(\omega)$ is defined as the first term in eq 8,[69]

$$\Lambda_{f,i}(\omega) = \frac{i\sigma_{f,i}(0)}{\omega - \omega_{f,i} + i\hat{\bar{W}}_{f,i;f,i}(\omega)} \quad (11)$$

This function is a Lorentzian line shape with a width determined by $Re[W_{f,i;f,i}(\omega)]$ and a shift in peak resonance determined by $Im[W_{f,i;f,i}(\omega)]$. The nonsecular terms in eq 10 are significant when the absorption line shapes corresponding to f, i and f', i' overlap to a meaningful degree and when the probability amplitude for bath-induced coupling between states f, i, f', and i' is large, as eqs 8 and 10 indicate.

IV. Results

A. APTCF Analysis of Solvated HCl. The spectral analysis of solvated HCl resulting from the APTCF approach is summarized in Figure 3a−f. Figure 3a illustrates the combined pulsed THz-FTIR data for gaseous HCl. The pulsed THz data extend from approximately 10 to 100 cm^{-1} (filled circles) and the FTIR data extend from approximately 60 to 300 cm^{-1} (open circles). The data are qualitatively fit by a rigid-rotator model (solid line); however, the absorbance levels of the data and the fitting function differ due to insufficient scan length in the time domain. The rigid-rotator model neglects centrifugal distortion effects on the resonance positions; hence, mismatch between data and the fit is evident above 200 cm^{-1}. The spacing between successive transitions is 20.8 cm^{-1} as indicated by the arrow in Figure 3a, which is twice the rotational B constant for the diatom HCl. The 40−280 cm^{-1} region of this spectrum has been measured previously.[57,58]

The effect of dissolving HCl in a liquid is illustrated by comparing the two normalized absorbance spectra in Figure 3b. The solid line is the gaseous HCl spectrum and the circles denote the decane solvated HCl spectrum. Clearly, the discrete rotational resonances evident in the gas phase spectrum are completely lost in solution. The APTCF line shape theory allows for quantitative analysis of the solute−solvent interactions. Figure 3c displays the series of theoretical, Lorentzian-like line shapes associated with the $\Delta j = \pm 1$ rotational transitions of solvated HCl overlaid on the theoretical spectrum of discrete resonances for gaseous HCl (heavy solid line). Each transition is strongly broadened and shifted by the interaction of HCl with the surrounding solvent molecules. Close examination of Figure 3c shows that the degree of broadening and peak-shifting of the individual resonances decreases with increasing j quantum number; the solute bath interaction decreases with increasing j. Transitions between low energy levels that reflect slow rotational motion allow more time for solute−bath interaction relative to transitions between high energy levels. Hence, the higher quantum number resonances are more sharply defined. It may also be that the bath interaction is weaker for the higher frequency transitions since the pure solvent (dipolar) spectral density (i.e. the IR spectrum) decreases beyond 70 cm^{-1}.

Figure 3d shows the theoretical line shapes associated with secular contribution to the absorption coefficient; each corresponds to one term in eq 9. Figure 3e illustrates the theoretical line shapes associated with the nonsecular contribution to the absorption coefficient. As shown in eq 10, the individual nonsecular line shapes are the product of two Lorentzian line shapes, $\Lambda_{f,i}(\omega)$ and $\Lambda_{f',i'}(\omega)$, weighted by the interference factor, $W_{f,i;f',i'}(\omega)$. Figure 3f illustrates the APTCF theoretical fit to the measured absorbance data for decane solvated HCl. The fit is the sum of the secular contributions of Figure 3d and the nonsecular contributions of Figure 3e.

B. Polarizability Dependence of Spectra. Figure 4a illustrates the pulsed THz (solid circles) and FTIR data (hollow circles) for the absorption coefficient spectrum of HCl dissolved in CCl_4 at 295K. The peak absorbance occurs at 141 cm^{-1} and the full-width at half-maximum (fwhm) of the band is 116 cm^{-1}. Figure 4b illustrates the FTIR data for HCl dissolved in $CHCl_3$ at 295 K. The comparatively broader peak occurs at 167 cm^{-1}, and the fwhm is 158 cm^{-1}. The larger degree of band broadening and peak shifting of HCl in $CHCl_3$, relative to CCl_4 reflects a stronger solute−solvent interaction. A computer code was written and used to generate the APTCF fitting function, the sum of eqs 9 and 10. For convenience of expression and to facilitate comparison with literature values, reduced values for the line shape function fitting parameters, the interaction strength and APTCF time constant, are used. The reduced interaction strength parameter λ^2 is related to the (nonreduced) interaction strength parameter λ^2_n as $\lambda^2 = \lambda^2_n/(B\hbar c)^2$ where B is the HCl rotational constant, $\hbar$ is Planck's constant, and c is the speed-of-light. Likewise, the reduced time constant τ_c is related to the nonreduced time constant, $\tau_{c,n}$, by $\tau_c = (2\pi Bc)\tau_{c,n}$.

Figure 5 illustrates solvent polarizability dependence of the measured absorbance spectra for HCl dissolved in solvents of high molecular symmetry Ar, Kr, Xe, SF_6, and CCl_4. (The spectral parameters for Ar, Kr, Xe, (and SF_6 solutions were taken from the literature.[33,54]) Both the frequencies of the peak positions and the full widths at half-maxima (fwhm) of the absorbance line shapes are observed to increase with solvent polarizability in a roughly linear fashion.

Figure 6a shows the solvent polarizability dependence of the reduced interaction strength parameters that characterize the line shape functions used to fit the far-infrared spectra of HCl solvated in the symmetric solvents. The polarizability values

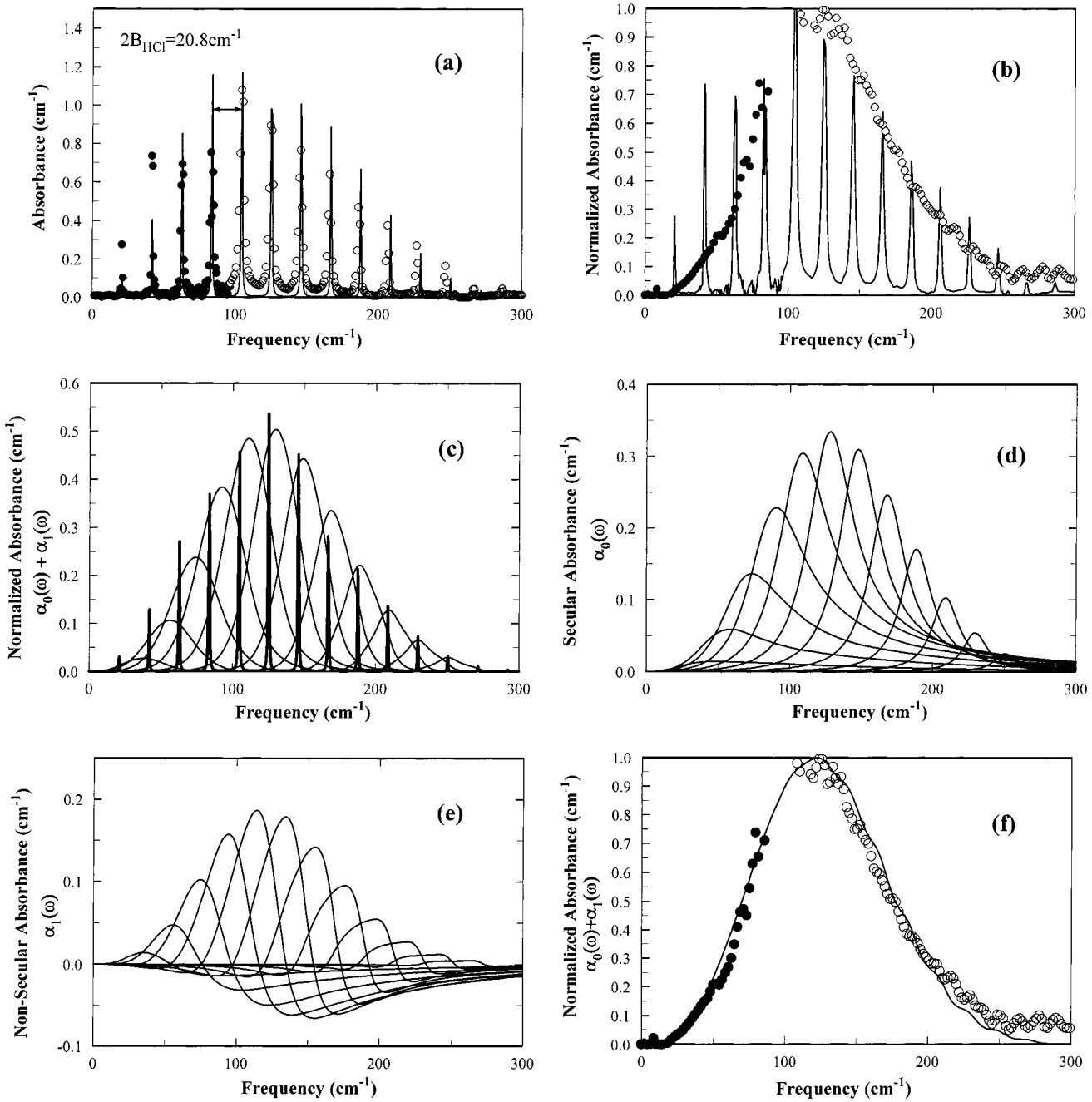

Figure 3. (a) The frequency dependent absorbance spectrum for gaseous HCl. The filled circles denote data acquired with the THz spectrometer and the open circles with the FTIR spectrometer. The solid black line denotes the fit generated by the quantum mechanical rigid rotator model. (b) The experimental normalized absorbance spectra for gaseous HCl (solid line) and for HCl dissolved in decane (circles). (c) The theoretical normalized absorbance spectra. The spectrum generated by the rigid rotator model HCl (heavy solid line) is overlaid on that generated by the APTCF model. (d) The series of secular line shapes associated with $\Delta j = \pm 1$ transitions between pure rotational levels. (e) The series of non-secular line shapes associated with $\Delta j = \pm 1$ pure rotational transitions. (f) The experimental absorbance spectra for HCl/decane fitted by the APTCF generated line shape. This fit is the sum of the line shapes presented in Figures 4d and e.

for these "spherical" solvents were taken from the literature.[59] The peak position and rotational widths for all HCl-solvent systems discussed herein, and the values for λ^2 and τ_c that are plotted in Figure 6a and b are listed in Table 1. The line shape fitting parameters for Ar, Kr, Xe, and SF_6 were taken from the literature.[33,54] The quadratic fit to the data points of Figure 6a is well-determined. The molecular polarizabilities of the alkane solvents were calculated from literature values of the refractive index by using the Lorentz−Lorenz equation: $(n - 1) = 2\pi\rho\alpha$ where n is the refractive index, ρ is the number density, and α is the molecular polarizability.[60] The error in the value of λ^2 for CCl_4 is denoted by the vertical error bars of ± 7 (reduced units), the amount the this parameter could be varied when fitting the data without noticeably changing the quality of the fit to the data.

Figure 6b displays the polarizability dependence of the anisotropic potential correlation time τ_c, which is a measure of the time scale for evolution of the configuration of solvent molecules about HCl. The best-fit values for τ_c increase with polarizabilty across the series; CCl_4 is an exception to the monotonic trend. The range over which τ_c for CCl_4 could be adjusted without significantly affecting the quality of the fit to the data is represented by the vertical error bars of ± 0.06 (reduced units).

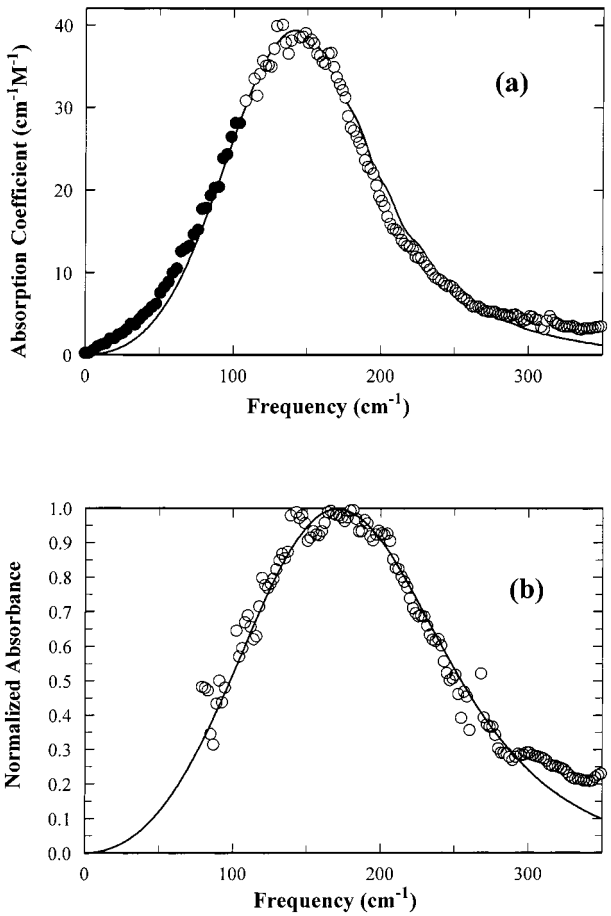

Figure 4. (a) The frequency dependent absorption coefficient spectrum for HCl in CCl_4. Data acquired with the THz spectrometer (solid circles) and with the FTIR spectrometer (open circles) are shown. The APTCF based fit to the experimental data (solid line) as characterized by the fitting parameters $\lambda^2 = 166$ and $\tau_C = 0.22$. (b) The normalized absorbance spectra for HCl in $CHCl_3$ where the symbols are the same as in Figure 4a and the APTCF model has parameters $\lambda^2 = 397$ and $\tau_C = 0.18$.

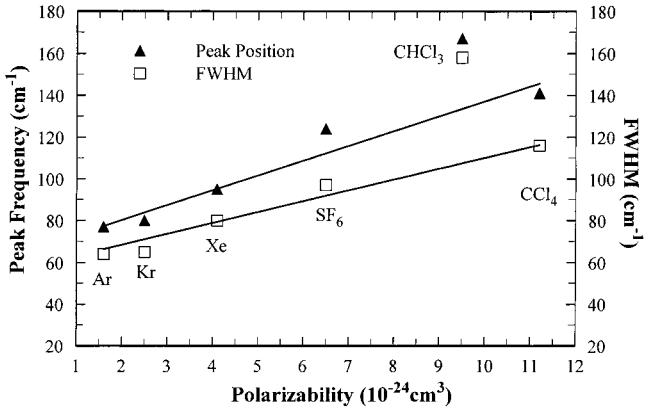

Figure 5. The absorbance peak widths and positions of the measured absorbance curves for the spherical solvent series plotted against the solvent polarizability.

Figure 7a and b illustrate the alkane solvated HCl spectra and the theoretical fits of the APTCF model. A computer program (written in C) was used to generate the APTCF fitting functions, the sum of eqs 9 and 10. The quality of the fit to pentane solvated HCl in Figure 7a suffers at low frequency because of the smaller THz absorbance and larger experimental noise both of which are caused by the low solubility of HCl in pentane. Therefore, the closeness of fit criteria for the THz (10−75 cm^{-1}) data was relaxed for HCl−pentane. An analogous but less severe effect occurs in the far-infrared spectral region (above 200 cm^{-1}) where only a small amount of radiation from the FTIR light source is absorbed. Therefore, the data in 75−200 cm^{-1} spectral region received the most attention in the process of fitting the APTCF absorbance curve to the pentane solvated HCl data. The closeness of the theoretical fit to the experimental data is improved for longer chain alkanes due to the higher signal-to-noise ratio of the solvated HCl spectra in systems where more concentrated HCl solutions were obtainable. The improved data quality is evident in the normalized absorbance spectrum of hexane solvated HCl shown in Figure 7b.

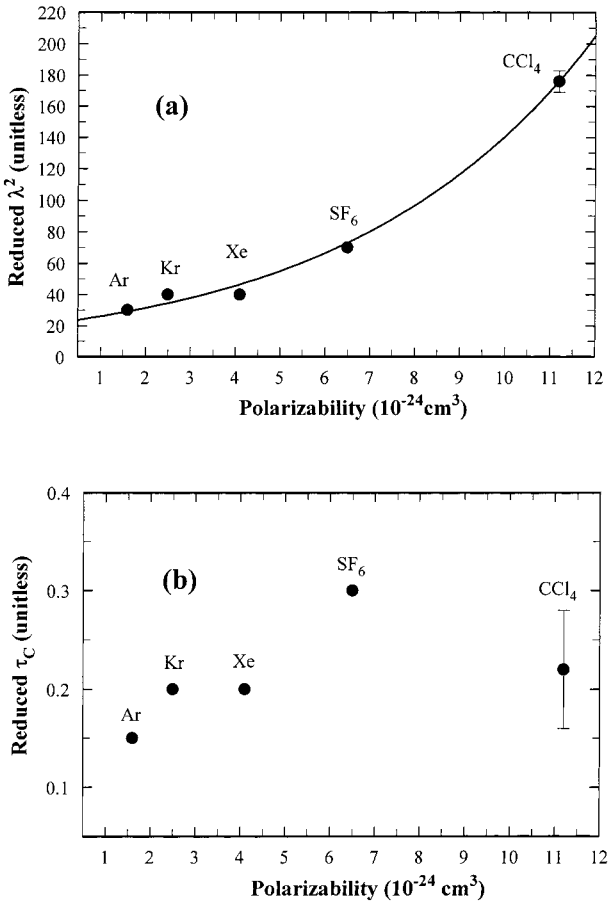

Figure 6. (a) The solute−solvent interaction strength plotted against the solvent polarizabilities for the symmetric series of solvents. The solid line denotes a NLLS quadratic fit ($R^2 = 0.99$) to the data. (b) The for the correlation time of the anisotropic potential plotted against the solvent polarizability.

The polarizability dependence for the mean square field parameter obtained in the alkane solvated HCl analysis is shown in Figure 8a. A trend of increasing λ^2 with increasing solvent polarizability is only weakly apparent. This dependence is fit by a quadratic function whose slope is 12 times smaller than the slope found in the analogous analysis of the symmetric solvent data. Hence, the dependence of λ^2 upon solvent polarizability, while strong in the symmetric solvent series, is very weak for the alkane series. The error associated with each of these points is ±7 (reduced units), the range over which this parameter could be varied when fitting the data without noticeably changing the quality of the fit to the data. The correlation time parameter used in the APTCF model is shown plotted against the solvent polarizability in Figure 8b and against the solvent viscosity in Figure 8c. The error associated with

TABLE 1: Spectral and Fitting Parameters for HCl Solutions[a]

solvent	peak (cm^{-1})	FWHM (cm^{-1})	λ^2 (unitless)	τ_C (unitless)	ρ ($\times 10^{22}$ mL^{-1})	ξ (10^{-24} cm^3)	η (cP)	T (K)
Ar	77	64	30	0.15	1.18	1.6	-	162.5
Kr	80	65	40	0.20	1.71	2.5	0.15	125
Xe	95	80	40	0.20	1.37	4.1	0.21	175
SF_6	124	97	70	0.30	0.78	6.5	-	273
CCl_4	141	116	175	0.10	0.62	11.2	0.91	295
$CHCl_3$	167	158	395	0.09	0.95	9.5	-	295
C_5H_{12}	116	105	64	0.04	0.52	10.9	0.23	295
C_6H_{14}	123	108	66	0.06	0.46	13.0	0.31	295
$C_{10}H_{22}$	123	106	69	0.06	0.31	21.1	0.89	295
$C_{16}H_{34}$	123	106	74	0.08	0.21	33.5	2.87	295

[a] All included information on HCl solvated in Ar, Kr, Xe, and SF_6 was taken from refs 63, 33, and 54.

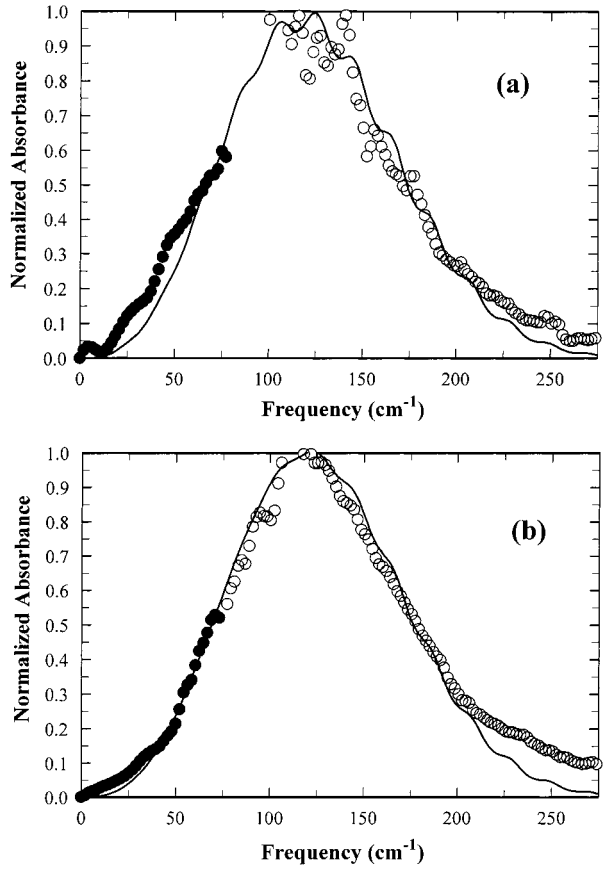

Figure 7. (a) The solid (THz data) and hollow circles (FTIR data) denote the experimental normalized absorbance spectra for HCl in pentane. The fit parameters for the solid line are $\lambda^2 = 63.7$ and $\tau_C = 0.038$. (b) The analogous spectrum for HCl solvated in hexane for which the APTCF fit parameters are $\lambda^2 = 66.5$ and $\tau_C = 0.60$.

each point is ±0.06 (reduced units). The values for λ^2, τ_c, the solvent polarizabilities, and solvent viscosities are listed in Table 1.

V. Discussion

A. Nonpolar Solvents with High Symmetry. Figure 5 illustrates the solvent polarizability dependence of the peak position and the full width at half-maximum (fwhm) of the measured absorbance spectra for HCl−spherical solvent solutions. The fitted curves illustrate the linear solvent polarizability dependence for both the peak position and fwhm data. The positive slopes indicate an increasing solute-bath interaction across the series.

A quadratic fit to the interaction parameter data (solid line in Figure 6) captures the polarizability dependence, and as shown in the Theory section, λ^2 is directly proportional to the mean-square field of the bath $\langle E^2 \rangle$. Assuming that the dominant term that gives rise to this bath field is due to dipole moments induced on the nondipolar solvent molecules by the permanent dipole moment on HCl, the field resulting from the bath would be expressed as

$$\vec{E}_{\text{bath}} \propto \sum_{\chi}^{\text{bath}} \frac{\vec{\mu}_{\text{ind},\chi}}{r_\chi^{\,3}} \tag{12}$$

where the sum runs over all the bath molecules, $\mu_{\text{Ind},\chi}$ is the dipole moment induced in the solvent molecule χ, and r_χ is the distance between HCl and the χth solvent molecule.[61] The induced dipole moment μ_{ind} is

$$\vec{\mu}_{\text{ind}} = \xi_{\text{bath}} \vec{E}_{\text{moment}} \tag{13}$$

where E_{Moment} is the electric field resulting from the permanent dipole moment on HCl and ξ_{bath} is the molecular polarizability of the bath. Additional polarization of the solvent molecules may occur as a result of induction by the hexadecapole moment on SF_6 and the octopole and hexadecapole moments on CCl_4 but these terms are assumed to be small. Therefore, the bath field is linearly dependent on the solvent polarizability, and, since $\lambda^2 = {}^1/_3\mu^2\langle E^2_{\text{bath}}\rangle$, $\lambda^2 \propto \xi^2_{\text{bath}}$. Hence, the quadratic fit to the values of λ^2 in Figure 7a is consistent with the dipole−induced dipole (DID) interaction between the solute and solvent for the spherical solvent series. In addition, this connection between ξ_{bath} and $\langle\lambda^2\rangle$ serves as a constraint on the range of values over which λ^2 may be varied for a given spherical solvent. Hence, the degree of uniqueness with which the nominally two adjustable parameter model is capable of fitting the solvated HCl absorbance data is increased.

Further evidence for the connection between λ^2 and the DID interaction is obtained through a comparison of HCl dissolved in $CHCl_3$, whose normalized absorbance spectrum is shown in Figure 4b. The larger peak shift (26 cm^{-1}) and band broadening (42 cm^{-1}) of the HCl/$CHCl_3$ spectrum relative to that for HCl/CCl_4 indicate that the solute−solvent interaction is significantly increased. This is due to the interaction of HCl with the permanent dipole (PD) moment of $CHCl_3$ (1.01 D in the gas phase) in addition to the DID interactions. In fact, by using the quadratic dependence of the DID interaction shown in Figure 6a, a determination of the relative magnitudes of the permanent dipolar and DID coupling strengths may be made. The polarizability value for chloroform ($9.0 \times 10^{-24}$$cm^3$) indicates that the DID component is 25% and the PD component is 72% of the total interaction strength represented by the fitting parameter $\lambda^2 = 397$. The constant offset, ~4%, reflected by the non-zero intercept probably results from repulsive interactions. Interest-

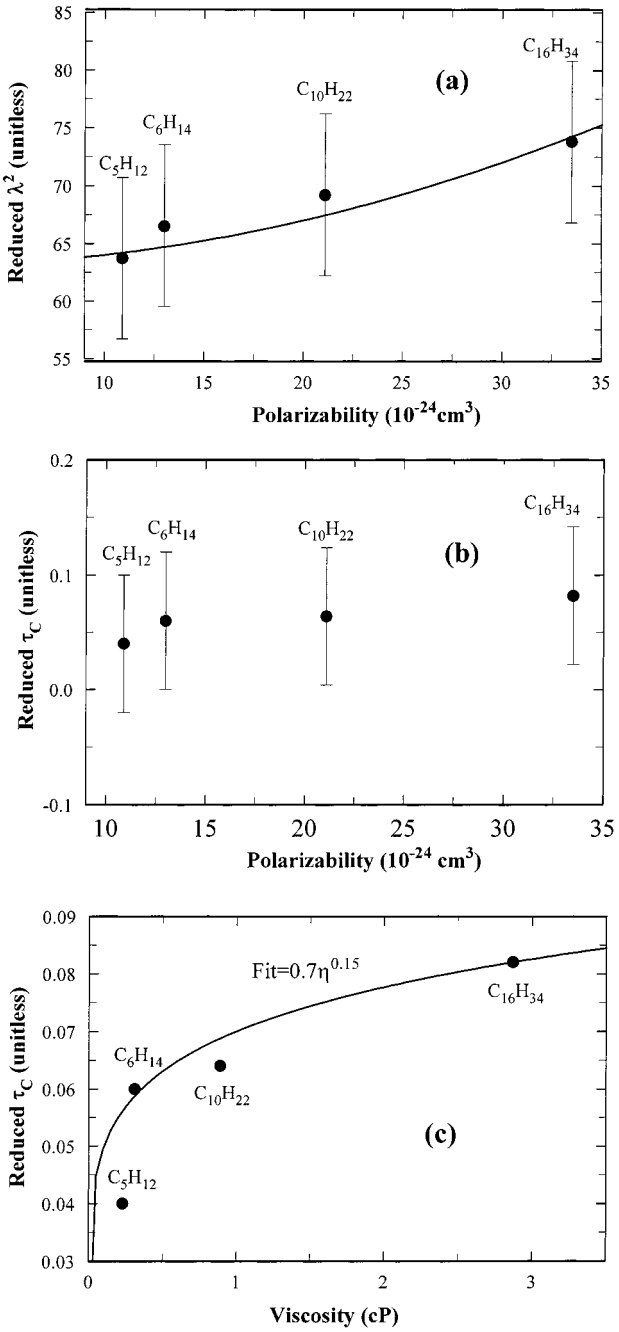

Figure 8. (a) The solute−solvent interaction strength plotted against the solvent polarizabilities for the alkane series of solvents. The solid line denotes a NLLS quadratic fit ($R^2 = 0.99$) to the data. Note that the *y*-axis spans the same range as that of Figure 6a. (b) The correlation time of the anisotropic potential plotted against the solvent polarizability. (c) The correlation time plotted against the solvent viscosity and fit by a power law model (solid line).

ingly, the DID and PD contributions to the total interaction strength are exactly the same magnitudes obtained in our earlier bi-Mori analysis of the THz spectrum of pure $CHCl_3$.[16] These terms were ascribed to longitudinal (for DID) and Debye (for PD) relaxations.

The solvent density, hence collision frequency, which is the classic parameter associated with spectral broadening,[62,63] is changing across the solvent series. However, the number densities for the symmetric solvents listed in Table 1 show that the number density is anticorrelated with the solvent polarizability, and therefore, with the interaction strength parameter. Therefore, the spherical solvent dependence for the interaction strength parameter must be due to a property of the solvent other than the number density.

A turnover in the solvent polarizability dependence of the best-fit values for the APTCF exponential time constant is evident in Figure 6b; the values for τ_c increase with solvent polarizability but decrease from SF_6 to CCl_4. It has been proposed that while undergoing rotation, HCl drags along part of the first shell of solvent molecules that surround it.[64] The dragging effect will increase τ_c because this coupled rotation of the first solvation shell tends to retain the leading terms in the anisotropic potential and, hence, lengthens the correlation time for the anisotropic potential. This phenomenon requires a strong electrostatic interaction between HCl and the surrounding solvent molecules that would have to increase with solvent polarizability to account for the data. However, since molecular polarizability increases with molecular volume, the size of highly polarizable molecules may counteract their tendency to be dragged by HCl; SF_6 is characterized as having a molecular radius of 5.51 Å while CCl_4 has a larger radius of 5.88 Å.[65] However, since CCl_4 is heavier than SF_6, the inertia for dragging CCl_4 is greater than that for SF_6. Hence, the turnover in the polarizability dependence of τ_c between SF_6 and CCl_4 (in Figure 6b) may reflect this notion of hindered molecular following. This conclusion is speculative and requires further investigation.

B. Nondipolar Solvents with Chainlike Geometries. The values for λ^2 and τ_c for the alkane solvated HCl systems shown in Figure 8 and listed in Table 1 are in strong contrast to the spherical solvent series in that there is almost no polarizability dependence. The slope is less than 1/10 that for the spherical solvent series. This polarizability independence is surprising in light of the broad polarizability range spanned by the alkanes ($\xi_{pentane} = 10.1 \times 10^{-24}cm^3$ and $\xi_{hexadecane} = 33.5 \times 10^{-24}cm^3$) relative to the spherical solvents and is suggestive of more subtle intermolecular interactions than the strong quadratic polarizability dependence observed for the spherical solvents.

The polarizability independence of λ^2 across the alkane solvent series can be explained as a *polarizability density* effect. The induction of dipole moments requires the combination of a polarizable material and an electric field. Because of the inverse cubic decay of the dipolar field, the polarizability of the nearest portions of the alkane molecules contribute most to the induced dipole moment strengths. Furthermore, the group polarizability values of those CH_2 and CH_3 groups that lie near HCl contribute to an effective molecular polarizability that is less than the nominal molecular polarizability value listed in Table 1. This decrease is most severe for the longer chain alkanes resulting in a saturation of the effective polarizability since the alkane molecules become longer than the distance over which the dipolar electric field induces significant polarization. Therefore, no polarizability dependence is observed because the polarizability per unit volume is constant for the alkane solvents.

The small values of λ^2 for the alkanes also follows, in part, from their characteristically low density. CCl_4, which interacts strongly with HCl, has a density of 6.2 molecules/nm^3. Assuming an approximate radius for the first solvation shell of 8 Å (based on molecular dynamics simulation of the pairwise radial distribution function for (H)Cl−Cl pairs),[66] the corresponding spherical volume is 2 nm^3. Hence, roughly 12 CCl_4 molecules can occupy this volume corresponding to that expected for a cubic close packed structure.[48] The alkanes, on the other hand, have much lower liquid densities. Decane, for example, has a density of 3.1 molecules/nm^3. Therefore, only six decane molecules fit in a spherical volume of 2 nm^3. The interaction energy between HCl and the solvent molecules in its first

solvation shell is simply the sum of the interaction energies between HCl and the individual solvent molecules in the shell. Therefore, the degree of solute−solvent interaction tends to increase with solvent number density. As Table 1 shows, the densities for the solvents in the alkane series do not vary widely across the series and all are rather small, less than 5.3 molecules/nm^3.

The weak polarizability dependence of τ_c for the alkane solution spectra is shown in Figure 8b. The solvent viscosity η dependence of τ_c for the alkane solution spectra, shown in Figure 8c, is qualitatively reproduced by a power law model with an exponent of 0.15. A similar nonlinear viscosity dependence has been observed in pressure dependent photoisomerization studies of *tert*-stilbene in various alkanes.[67] This similarity implies that, to some extent, τ_c characterizes the solvent response to an isomerization reaction. The data in Figure 8c imply that the isomerization rate should decrease across the alkane series at equal temperature and pressure as seen in experiment.[68,67] However, the error of ± 0.06 (reduced units) associated with each value for τ_c is significant. Hence, additional study is required to develop the connection between τ_c and the solvent response to reaction.

VI. Conclusions

Evidence for different types of DID interactions for spherical and linear nondipolar solvents reveal a subtle aspect of the solvation process for the HCl probe. The linear solvents are long relative to the length scale of the HCl dipolar electric field such that only the part of the molecule nearest the dipolar solute is polarized. The inhomogeneity of the electric field strength across the molecular dimension suggests an inhomogeneity in the response of an individual solvent molecule to the solute dynamics. The electrostatic solvent response of linear molecules may be "submolecular" in that the dissipation of free energy of the reaction-induced nonequilibrium configuration occurs largely through motion of the nearest portions of the linear molecules. The more distant portions of the solvent molecule move under the force exerted by the near molecular portion to which they are connected. This concept implies that the solvent response is electrostatic at short distances and mechanical for longer distances.

The ability to generate and detect more energetic THz pulses might allow nonlinear THz spectroscopies to be applied to solutions. Terahertz hole burning or echo experiments, for example, would provide information on the homogeneous dephasing times associated with pure rotational motion. Analysis of such data would be straightforward, as APTCF theory predicts values for T_1 and T_2 population relaxation and dephasing times. Hence, these time-resolved nonlinear spectroscopies could provide quantitative detail on the bath modes that couple significantly to the solute. A related aspect of this problem involves the elucidation of the extent to which Raman-active and dipolar-active solvent modes are coupled. This discrimination would be valuable in the attempt to determine the mechanism of solvation because it would establish "selection rules" that proposed molecular interactions would be required to obey. These experimental methods represent a unique perspective for elucidating a molecular picture of solvation. This research is currently underway.

Acknowledgment. This paper is dedicated to Kent Wilson specifically as a response to a conversation that he and one of us (N.F.S.) had at UCSD in 1991 on the topic of rotational motion in liquids. We thank Kent for sharing his uniquely inspirational approach to science and heartfelt dedication as mentor to so many of a younger generation. We acknowledge financial support from the NIH (Grant RO1−GM57768), NSF (Grant CHE-9357424), and NSF (Grant PHY-9731201). N.F.S. acknowledges the David and Lucile Packard, Camile Dreyfus, and Alfred P. Sloan Foundations for fellowships.

References and Notes

(1) Adelman, S. A. *Adv. Chem. Phys.* **1983**, *53*, 61.
(2) Lee, L. L.; Li, Y. S.; Wilson, K. R. *J. Chem. Phys.* **1991**, *95*, 2458.
(3) Gertner, B. J.; Whitnell, R. M.; Wilson, K. R.; Hynes, J. T. *J. Am. Chem. Soc.* **1991**, *113*, 74.
(4) Raferty, D.; Sension, R. J.; Hochstrasser, R. M. Chemical aspects of solution phase reaction dynamics. In *Activated Barrier Crossing*; Fleming, G. R., Hanggi, P., Eds.; World Scientific: River Edge, NJ, 1993; p 163.
(5) Cho, M.; Hu, Y.; Rosenthal, S. J.; D. C. Todd, M. D.; Fleming, G. R. Friction effects and barrier crossing. In *Activated Barrier Crossing*; Fleming, G. R., Hanggi, P., Eds.; World Scientific: River Edge, NJ, 1993; p 143.
(6) Schroeder, J.; Troe, J. Solvent effects in the dynamics of dissociation, recombination and isomerization reactions. In *Activated Barrier Crossing*; Fleming, G. R., Hanggi, P., Eds.; World Scientific: River Edge, NJ, 1993; p 206.
(7) Dellago, C.; Bolhuis, P. G.; Chandler, D. *J. Chem. Phys.* **1999**, *110*, 6617.
(8) Ronne, C.; Astrand, P. O.; Keiding, S. R. *Phys. Rev. Lett.* **1999**, *82*, 2888.
(9) Heilweil, E. J. Far-Infrared Spectroscopy of Proteins, DNA and Hydrogen-Bonded Systems. Presented at the APS March Meeting, 1998, Los Angeles.
(10) Einstein, A. *Ann. Phys.* **1905**, *17*, 549.
(11) Langevin, P. *Compt. Rend.* **1908**, *146*, 530.
(12) Debye, P. *Polar Molecules*; Dover: New York, 1929.
(13) Zwanzig, R. *J. Chem. Phys.* **1960**, *33*, 1338.
(14) Mori, H. *Prog. Theor. Phys.* **1965**, *34*, 399.
(15) Pedersen, J. E.; Keiding, S. R. *IEEE J. Quantum Electron.* **1992**, *28*, 2518.
(16) Flanders, B. N.; Cheville, R. A.; Grischkowsky, D.; Scherer, N. F. *J. Phys. Chem.* **1996**, *100*, 11824.
(17) Kindt, J. T.; Schmuttenmaer, C. A. *J. Phys. Chem.* **1996**, *100*, 10373.
(18) Thrane, L.; Jacobsen, R. H.; Jepsen, U.; Keiding, S. R. *Chem. Phys. Lett.* **1995**, *240*, 330.
(19) Stratt, R. Private communication.
(20) Haran, G.; Wynne, K.; Hochstrasser, R. M. *Chem. Phys. Lett.* **1997**, *274*, 365.
(21) McElroy, R.; Wynne, K. *Phys. Rev. Lett.* **1997**, *79*, 3078.
(22) Venables, D. S.; Schmuttenmaer, C. A. Time-Resolved Studies of Liquid Dynamics. In *Ultrafast Phenomena XI*; Zinth, W., Fujimoto, J. G., Eds.; Garmisch-Partenkirchen Germany, 1998; p 565.
(23) Flanders, B. N.; Scherer, N. F. "Optical pump-terahertz probe spectroscopy of condensed phase reaction dynamics". Presented at the Photonics West Meeting of the International Society for Optical Engineering, 1998, San Jose, CA.
(24) Kindt, J. T.; Schmuttenmaer, C. A. *J. Chem. Phys.* **1999**, *110*, 8589.
(25) Chandler, D. *Introduction to Modern Statistical Mechanics*; Oxford University Press: New York, 1987.
(26) McQuarrie, D. *Statistical Mechanics*; Harper Collins: New York, 1976.
(27) Harde, H.; Katzenellenbogen, N.; Grischkowsky, D. *Phys. Rev. Lett.* **1995**, *74*, 1307.
(28) Harde, H.; Cheville, R. A.; Grischkowsky, D. *J. Phys. Chem. A* **1997**, *101*, 3646.
(29) Mori, H. *Prog. Theor. Phys.* **1965**, *33*, 423.
(30) Zwan, G. v. d.; Hynes, J. T. *J. Phys. Chem.* **1985**, *89*, 4181.
(31) Breton, J.; Hardisson, A.; Mauricio, F.; Velasco, S. *Phys. Rev. A* **1984**, *30*, 542.
(32) Breton, J.; Hardisson, A.; Mauricio, F.; Velasco, S. *Phys. Rev. A* **1984**, *30*, 553.
(33) Hernandez, A. C.; Velasco, S.; Mauricio, F. *Phys. Rev. A* **1985**, *31*, 3419.
(34) Li, Y. S.; Wilson, K. R. *J. Chem. Phys.* **1990**, *93*, 8821.
(35) Fellers, R. S.; Leforestier, C.; Braly, L. B.; Brown, M. G.; Saykally, R. J. *Science* **1999**, *284*, 945.
(36) Pshenichnikov, M. S.; de Boeij, W. P.; Wiersma, D. A. *Opt. Lett.* **1994**, *19*, 572.
(37) Voehringer, P.; Westervelt, R. A.; Yang, T. S.; Arnett, D. C.; Feldstein, M. J.; Scherer, N. F. *J. Raman Spectrosc.* **1995**, *26*, 535.
(38) Arnett, D. C.; Voehringer, P.; Scherer, N. F. *J. Am. Chem. Soc.* **1995**, *117*, 12262.

(39) Flanders, B. N.; Arnett, D. C.; Scherer, N. F. *IEEE J. Sel. Top. Quantum Electron.* **1998**, *4*, 353.
(40) Krausz, F.; Spielmann, C.; Brabec, T.; Witner, E.; Schmidt, A. *Opt. Lett.* **1992**, *17*, 204.
(41) Asaki, M. T.; Huang, C. P.; Garvey, D.; Zhou, J.; Kapteyn, H. C.; Murnane, M. M. *Opt. Lett.* **1993**, *18*, 977.
(42) Katzenellenbogen, N.; Grischkowsky, D. *Appl. Phys. Lett.* **1991**, *58*, 222.
(43) Ralph, S. E.; Grischkowsky, D. *Appl. Phys. Lett.* **1991**, *59*, 1972.
(44) This requirement of loose focusing in order to decrease the photogenerated carrier density in the semiconducting material is consistent with the findings of an earlier study in which looser focusing of energetic, cavity-dumped pulses (relative to output-coupled pulses) was required in order to prevent circuit burnout of the F-chip source.
(45) You, D.; Jones, R. R.; Bucksbaum, P. H.; Dykaar, D. R. *Opt. Lett.* **1992**, *18*, 290.
(46) Wu, Q.; Litz, M.; Zhang, X. C. *Appl. Phys. Lett.* **1996**, *68*, 2924.
(47) Gallot, G.; Zhang, J.; McGowan, R. W.; Jeon, T.; Grischkowsky, D. *Appl. Phys. Lett.* **1999**, *74*, 3450.
(48) Galatry, L.; Robert, D. *Spectrochim. Acta* **1968**, *25A*, 1693.
(49) Miziolek, A. W.; Pimentel, G. C. *J. Chem. Phys.* **1976**, *65*, 4462.
(50) Gordon, R. G. *Adv. Magn. Reson.* **1968**, *3*, 1.
(51) Tolman, R. C. *The Principles of Statistical Mechanics*; Oxford University Press: London, 1938.
(52) Schatz, G. C.; Ratner, M. A. *Quantum Mechanics in Chemistry*; Prentice-Hall: Englewood Cliffs, 1993.
(53) Redfield, A. G. *Adv. Magn. Reson.* **1966**, *1*, 1.
(54) Roco, J. M. M.; Hernandez, A. C.; Velasco, S. *J. Chem. Phys.* **1992**, *97*, 5323.
(55) Zare, R. N. *Angular Momentum: Understanding Spatial Aspects in Chemistry and Physics*; Wiley-Interscience: New York, 1988.
(56) Ross, S. L. *Introduction to Ordinary Differential Equations*; John Wiley & Sons: New York, 1989.
(57) Datta, P.; Barrow, G. M. *J. Chem. Phys.* **1965**, *43*, 2137.
(58) Robert, D.; Galatry, L. *Chem. Phys. Lett.* **1968**, *1*, 526.
(59) *Handbook of Chemistry and Physics*; 74th ed.; Lide, D. R., Ed.; The Chemical Rubber Publishing Company: Boca Raton, 1994.
(60) Gray, C. G.; Gubbins, K. E. *Theory of Molecular Fluids*; Clarendon Press: Oxford, 1984; Vol. 1: Fundamentals.
(61) Griffiths, D. J. *Introduction to Electrodynamics*, 2nd ed.; Prentice Hall: Englewood Cliffs, New Jersey, 1989. The orientational dependence of the bath field on the induced solvent dipole moment is not shown in eq 21.
(62) Fano, U. *Phys. Rev.* **1963**, *131*, 259.
(63) Medina, A.; Velasco, S.; Hernandez, A. C. *Phys. Rev. A* **1991**, *44*, 3023.
(64) Rothschild, W. G. *Dynamics of Molecular Liquids*; John Wiley & Sons: New York, 1984.
(65) Hirschfelder, J. O.; Curtis, C. F.; Bird, R. B. *Molecular Theory of Gases and Liquids*; Wiley: New York, 1954.
(66) Chang, T. M.; Peterson, K. A.; Dang, L. X. *J. Chem. Phys.* **1995**, *103*, 7502. The (H)Cl−Cl radial distribution function was calculated from molecular dynamics data. The molecular dynamics simulation of HCl in CCl4 (Flanders, Moore, Scherer, Klein, unpublished results) was done using intermolecular parameters from T. M. Chang.
(67) Voehringer, P. Reaktionsdynamik von S_1−Photoisomerisierungen in Loesung: Temperatur- und Druckabhaengigkeit. Ph.D. Thesis, Georg-August-Universitaet zu Goettingen, 1991.
(68) Schroeder, J.; Troe, J.; Voehringer, P. *Chem. Phys. Lett.* **1993**, *203*, 255.
(69) Note that "*i* " in eq 9 is the summation index and refers to the rigid rotor eigenstate.